Ionospheric currents and field-aligned currents generated by dynamo action in an asymmetric Earth magnetic field

P. Le Sager and T. S. Huang

Prairie View Solar Observatory, Prairie View A&M University, Prairie View, Texas, USA

Received 13 July 2001; revised 28 August 2001; accepted 29 August 2001; published 14 February 2002.

[1] To investigate the influence of the magnetic field configuration on large-scale ionospheric electrodynamics, a geomagnetic field coordinate system based on Euler potentials is built for three magnetic field configurations: dipole, tilted dipole, and a revision of the International Geomagnetic Reference Field (IGRF). The two-dimensional ionospheric dynamo equation is expressed in this framework under the assumptions of equipotential field lines and conservation of current, including horizontal ionospheric conduction current and interhemispheric magnetic-field-aligned current. Equinoctial symmetric conductivity and neutral wind distributions are used to isolate the effects of the magnetic asymmetry about the geographic equator. In the case of the IGRF only, the coupling along realistic field lines permits the reproduction of an equinox local time shift between horizontal-current foci at all universal times. This is likely to explain the shift between the focus local times of *Sq* vortices that has been observed at equinox and at all universal times. The asymmetry due to nondipolar geomagnetic field distortions is found to be as efficient as conductivity and neutral wind asymmetries, which have been previously modeled, in driving Birkeland currents with an order of magnitude of 10^{-8} A m^{-2}. The magnetic field asymmetry also turns out to be as important as wind and conductance asymmetries to specify the Birkeland current pattern. *INDEX TERMS:* 2409 Ionosphere: Current systems (2708); 2427 Ionosphere: Ionosphere/atmosphere interactions (0335); 2437 Ionosphere: Ionospheric dynamics; 2443 Ionosphere: Midlatitude ionosphere; *KEYWORDS:* ionospheric dynamo, current system, Birkeland current, ionosphere/atmosphere interaction, magnetic coordinates

1. Introduction

[2] By neglecting pressure gradient in the magnetosphere and focusing on closed magnetic field lines, the electrodynamic coupling between the magnetosphere and the ionosphere-thermosphere system is commonly reduced to an ionospheric dynamo. In this ionosphere-thermosphere electrodynamics system the neutral wind induces a transport, via collisions, of ionospheric ions across the Earth magnetic field. Ionospheric currents and electric fields created by this dynamo effect have been investigated through numerical simulation models for almost 5 decades. Models take specified distributions of conductivities, neutral winds, and geomagnetic field and then solve the dynamo equation. Although they have been reasonably successful in reproducing the types of magnetic perturbations that are produced by ionospheric currents, they have been less successful in simulating electric fields and the regular variations of equivalent current with season and universal time (see reviews by *Wagner et al.* [1980] and *Richmond* [1989, 1995b]).

[3] Numerous improvements have been introduced in the models to reduce discrepancies between their predictions and observations. Efforts have principally concentrated on the refinement of conductivity and neutral wind distributions. It is done by taking the feedback on neutral dynamics into account [e.g., *Richmond et al.*, 1976], by incorporating experimental-data-based distributions [*Haerendel et al.*, 1992; *Eccles*, 1998] or sophisticated self-consistent plasma distribution [*Crain et al.*, 1993]. While the magnetic field configuration is also known to influence the simulation results, the Earth magnetic field has been usually reduced to a dipole for simplicity. Few works have investigated the role of its nondipolar distortions in the dynamo process, and the full implications of the real magnetic field remain to be determined, despite the qualitative contributions provided by *Wagner et al.* [1980].

[4] Use of a realistic magnetic field model for ionospheric work has two consequences that modify simulation results. First, it is recognized that taking into consideration the coupling between both hemispheres along the highly conducting magnetic field lines is needed to explain observations [*Wagner et al.*, 1980]. The effects of this coupling strongly depend on the magnetic field configuration. Second, a realistic field modulates the conductivity tensor (through its dependence on electron and ion gyrofrequencies) and the dynamo electric field $\mathbf{u}\times\mathbf{B}$, where $\mathbf{u}$ is the neutral wind.

[5] *Stening* [1971, 1973, 1977, 1981] has already introduced these changes in conductivity tensor and dynamo electric field $\mathbf{u}\times\mathbf{B}$ induced by the International Geomagnetic Reference Field (IGRF) 1965. Although his model allows for current flow along the magnetic field lines between both hemispheres, this coupling is performed with the help of dipole field lines. Thus a part of the strong organization of ionospheric phenomena by the magnetic field has not been taken into account, as illustrated by the equatorial electrojet. The latter is formed at the geographic equator rather than at the magnetic dip equator. Nevertheless, the modulations due to the longitudinal variations of the Earth's main magnetic field have been shown to account for many of the longitudinal variations in the *Sq*system [*Stening*, 1971, 1973].

[6] On the other hand, *Takeda* [1982] and *Richmond and Roble* [1987] explore differences associated only with the tilt of the dipole by solving the relevant partial differential equation of ionospheric dynamo. Within a tilted dipole configuration, electrodynamics calculations are easily carried out in a magnetic-field-oriented coordinate system, allowing for a coupling between the magnetic hemispheres instead of the geographic hemispheres. Both papers compare results for two different universal times (UT). They both present little UT differences in electric potential that show up when its gradients are taken to compute electric field

0148-0227/02/2001JA000211$09.00

and drift velocity. Electric currents eventually exhibit greater UT variability due to the tilt of the dipole.

[7] This variability argues for the use of a realistic Earth magnetic field model to simulate the coupling between hemispheres and more generally between ionosphere and magnetosphere. This is also supported by an experimental point of view. By providing longitude coverage, satellite observations give new insights into ionospheric electrodynamics [*Coley et al.*, 1990; *Fejer et al.*, 1995; *Maynard et al.*, 1995].Two satellites, San Marco D [*Maynard et al.*, 1995] and AE-E [*Fejer et al.*, 1995], present longitudinal ion drift variations, analysis of which requires consideration of departures of the geomagnetic field from dipolar configuration. A realistic magnetic field is also needed to investigate and separate the longitudinal and UT variations observed on the equivalent current [*Malin and Gupta*, 1977; *Wagner et al.*, 1980].

[8] One model exists that integrates dynamo processes in a realistic geomagnetic field frame. This is the thermosphere-ionosphere-electrodynamics general circulation model (TIE-GCM), which is not limited to the ionospheric wind dynamo but self-consistently computes the dynamics of the thermosphere and the ionosphere in three dimensions [*Richmond et al.*, 1992]. The magnetic frame is based on magnetic apex coordinates, for which electrodynamic equations have been derived [*Richmond*, 1995a]. The focus is put on the feedback of ionospheric dynamics on thermosphere dynamics and composition. It has been pointed out that ion-drag effects on the neutral dynamics are asymmetric about the geographic equator, leading to asymmetry in the wind and temperature distributions, even for the symmetric solar-UV forcing present at equinox. The asymmetric feedback on the thermosphere is another consequence of the use of realistic magnetic field, and it affects the dynamo in return. For the dynamo itself, it represents an indirect modulation of the neutral wind by the magnetic field. Thus the equinox asymmetry observed is due to a complex combination of wind, conductivities and dynamo emf $\mathbf{u} \times \mathbf{B}$ asymmetries and to the nondipolar coupling along magnetic field lines. However, the resulting asymmetry in the current system has not been examined, and there is need for simplified models for the transparency in cause and effect relationships.

[9] The present paper examines how the magnetic field affects the dynamo current system when neutral wind and conductivity modulations by the magnetic field are not taken into account. In other words, the magnetic influence is reduced to the direct modulation of the dynamo electric field $\mathbf{u} \times \mathbf{B}$ and to the coupling along magnetic field lines. A dynamo model has been developed to compare the numerical results obtained with a dipole, a tilted dipole, and a realistic magnetic field configuration. The latter is represented by the IGRF 1995 model [*IAGA*, 1996], and a coordinate system based on Euler potentials α and β has been constructed for each magnetic configuration (Section 2). Euler potentials, which are solely defined by the field, remain constant along a field line and provide a convenient magnetic coordinate system. The dynamo equation in these coordinates is derived in Section 3, along the model outlines. Quasi-static large-scale electrodynamic conditions are assumed and justified by observations of magnetic field perturbations during quite conditions. Magnetospheric currents are neglected, except Birkeland currents that can flow from one ionospheric hemisphere to the other, assuming infinite conductivity along equipotential field lines. The dynamo equation, a two-dimensional elliptical differential equation for the electric potential, is numerically solved on a 101 $\times$ 60 grid of normalized α and β coordinates. In section 4, uniform conductances, a simple zonal neutral wind, and a dipole configuration, for which an analytical solution exists, are used to validate our code. In section 5, simulation results obtained for the three magnetic configurations are compared under realistic neutral wind and conductance distributions. Because these distributions are symmetric about the geographic equator at equinox, asymmetric effects due to the sole magnetic field are investigated. They are compared with asymmetric effects due to the tilt of the dipole or to solstice distributions that have been previously modeled [*Maeda*, 1974; *Stening*, 1977; *Richmond and Roble*, 1987; *Takeda*, 1982, 1990]. Important results for the equinox local time shift between horizontal current foci and for the induced field-aligned currents are eventually derived.

2. The α, β Coordinate System

[10] To study influence of the magnetic field configuration on the ionospheric dynamo, results obtained with three different field models (dipole, tilted dipole, and a realistic field) have to be compared. Such comparisons are possible if results are expressed in geographical coordinates. However, it is convenient to construct models in a coordinate system aligned with the geomagnetic field, because of its strong influence on charged-article motion and then of its natural organization of ionospheric phenomena. This organization is particularly found in the coupling between magnetic hemispheres, which is performed along field lines: Electric potential and field-aligned currents at the north footprint of a field line are related to those at the south footprint of the same field line.

[11] *Richmond* [1995a] proposed two magnetic coordinate systems related to magnetic apex coordinates, the modified apex coordinates, and the quasi-dipole coordinates. A system based on Euler potentials is used in the present paper. Usually called α and β coordinates, Euler potentials remain constant along a geomagnetic field line and provide a proper magnetic coordinate system aligned with respect to the Earth main field.

[12] For the realistic Earth main field, we adopt a 1995 revision of the IGRF [*IAGA*, 1996]. The magnetic potential $V_m(r, \theta, \varphi)$ is expressed as a spherical harmonic expansion:

$$V_m = R_E \sum_{n=1}^{N} \sum_{m=0}^{n} \left(\frac{R_E}{r}\right)^{n+1} \left(g_n^m \cos(m\varphi) + h_n^m \sin(m\varphi)\right) P_n^m(\cos\theta), \quad (1)$$

where R_E is the mean radius of the Earth (6371.2 km), r is the radial distance from the center of the Earth, φ is the longitude eastward from Greenwich, θ is the geocentric colatitude, g_n^m and h_n^m are the spherical harmonic (Gauss) coefficients, P_n^m are the normalized associated Legendre functions, and N is the maximum spherical harmonic degree of the expansion, equal to 10.

[13] Observations state that ionospheric and magnetospheric currents induce magnetic perturbations that remain under 5% during quite daily conditions. Thus the magnetic field at ionospheric altitude can be expressed as the sum of the Earth main field $\mathbf{B} = -\nabla V_m$ and an additional component $\Delta\mathbf{B}$, which is considered as a little perturbation and is produced by currents external to the Earth. Under these conditions of magnetic quiescence, Euler potentials α and β can be calculated from the Earth main magnetic field. They are related to $\mathbf{B}$ by

$$\mathbf{B} = \nabla\alpha \times \nabla\beta = -\nabla V_m. \quad (2)$$

Their derivation is easy for a dipolar magnetic field but is rather difficult for any type of magnetic field. However, they can be numerically computed by different methods. In the present work, they are derived following the method presented by *Ho et al.* [1997] in the case of Neptune. Lines of constant α value and lines of constant β value are first determined on the zero scalar potential surface, starting with dipole approximations for the region far away from the planet and then using the equivalence between magnetic flux and area in Euler coordinates:

$$\Delta\alpha \ \Delta\beta = \mathbf{B} \ \Delta S, \quad (3)$$

where $\Delta\alpha$ and $\Delta\beta$ are ranges of α and β that bound the element area ΔS.

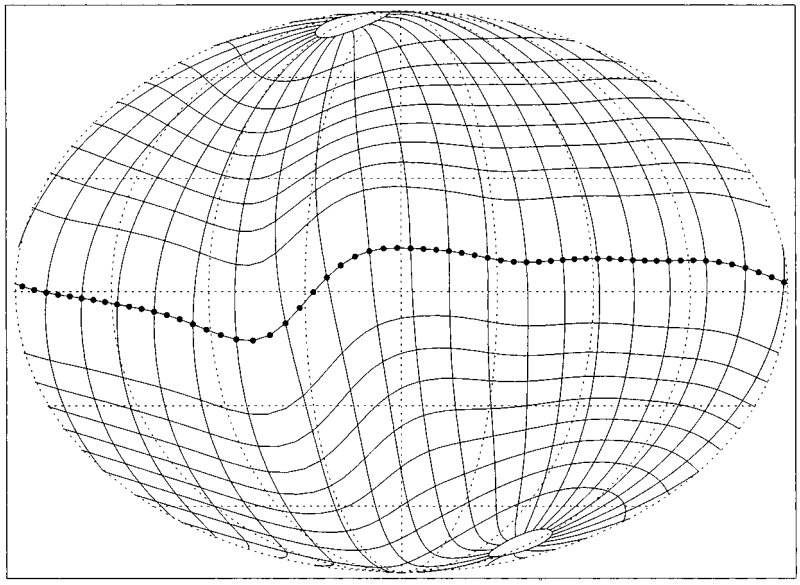

Figure 1. Sample of constant normalized α and β lines on the Earth surface for the International Geomagnetic

[14] For a dipole, α value is inversely proportional to the equatorial distance of the field line and β value is equal to the longitude (see equations (20a) and (20b) below). In the case of IGRF, the nondipolar components deform this simple relationship. Typically, the two footprints of a field line, defined by constant values of α and β, have different geographic longitude and latitude. With IGRF (1995), the α value along the magnetic equator on Earth's surface is not constant. Values of α along each β line are linearly renormalized in order that normalized α values are 100 at the magnetic dip equator on Earth's surface. From here and for simplicity, α will stand for renormalized α. In our model, 100 uniformly spaced α values (from 1 to 100) are eventually selected along 60 uniformly spaced β lines. Using $\mathbf{B} \times d\mathbf{l} = 0$, where $d\mathbf{l}$ is the increment along he field line, and using the constancy of α and β on each field line, the set of (α, β) Euler potentials is mapped onto the Earth surface. This mapping provides north and south conjugate footprint coordinates: ($\theta_N(\alpha, \beta)$, $\varphi_N(\alpha, \beta)$) and ($\theta_S(\alpha, \beta)$, $\varphi_S(\alpha, \beta)$). Each couple (α,β) corresponds with two footprints that will be linked in our ionosphere model. A regular sample of the footprints obtained with IGRF (1995) is displayed in Figure 1, where it is seen that the gradients of the magnetic coordinates are not at mutual right angles. There is then need for computation of the partial derivatives $\partial\alpha/\partial\theta$, $\partial\alpha/\partial\varphi$, $\partial\beta/\partial\theta$, and $\partial\beta/\partial\varphi$ at ionospheric altitude and at each footprint. They are numerically determined for each hemisphere when α and β coordinates are mapped onto the Earth surface. A discrete coordinate system aligned with the main geomagnetic field is eventually completed. The following description of our ionospheric dynamic model clarifies how electrodynamics calculations are carried out in this frame.

3. Ionospheric Electrodynamics: Basic Equations and Hemisphere Coupling

[15] *Vasyliunas* [1970] derived a general theoretical frame for modeling the magnetosphere-ionosphere coupling. By neglecting plasma pressure gradient effects in the magnetosphere and focusing on the closed part of the magnetosphere, in which magnetic field lines connect from one hemisphere to the other, the coupling is reduced to the ionospheric dynamo, which represents the electrodynamic coupling with the thermosphere. *Richmond* [1995a] developed equations of this dynamo for a general geomagnetic field configuration, with specific application to coordinate systems based on magnetic apex coordinates. In this section we derive these equations for the α,β coordinate system in order to develop a two-dimensional potential equation from assumptions of equipotential field lines and current continuity for quasi-static large-scale electrodynamics conditions.

3.1. Shell Ionosphere

[16] The response of the ionosphere to the electromagnetic field can be represented by the generalized Ohm's law in the rotating frame:

$$\mathbf{j} = \sigma_0 \mathbf{E}_{\parallel} + \sigma_P (\mathbf{E} + \mathbf{u} \times \mathbf{B})_{\perp} + \sigma_H \mathbf{b} \times (\mathbf{E} + \mathbf{u} \times \mathbf{B}), \qquad (4)$$

where $\mathbf{j}$ is the current density, σ_P, σ_H, and σ_0 are the Pedersen, Hall, and parallel conductivities, respectively, $\mathbf{u}$ is the neutral wind velocity, $\mathbf{E}$ is the electric field, and $\mathbf{b}$ is the unit vector parallel to $\mathbf{B}$. Subscripts // and $\perp$ correspond to components parallel and perpendicular, respectively, to $\mathbf{B}$. Under quasi-static conditions, $\mathbf{E}$ can be represented by an electric potential Φ: $\mathbf{E} = -\nabla\Phi$, and the current density is divergence-free.

[17] By imposing $j_r = 0$ in (4) to determine E_r and then an infinite σ_0, the ionosphere can be reduced to a two-dimensional medium upon integrating j_θ and j_φ along field lines and through the ionosphere conducting layer. The integrated horizontal current $\mathbf{J_H}$ in the thin shell ionosphere surrounding the Earth satisfies

$$\mathbf{J_H} = \Sigma \mathbf{E} + \mathbf{J}_w, \qquad (5)$$

where $\mathbf{J}_w$ is the current part due to the neutral wind $\mathbf{u}$ and Σ is the conductance tensor:

$$\begin{cases} J_{w\theta} = B\left(\frac{\cos^2\xi}{\cos\chi} + \sin^2\xi\cos\chi\right)\Sigma_P u_\varphi - B\left(\sin\xi\cos\chi\left(\frac{1}{\cos\chi} - \cos\chi\right)\Sigma_P - \Sigma_H\right)u_\theta \\ J_{w\varphi} = B\left(\sin\xi\cos\chi\left(\frac{1}{\cos\chi} - \cos\chi\right)\Sigma_P + \Sigma_H\right)u_\varphi - B\left(\frac{\sin^2\xi}{\cos\chi} + \cos^2\xi\cos\chi\right)\Sigma_P u_\theta \end{cases} \qquad (6)$$

$$\Sigma = \begin{pmatrix} \Sigma_{\theta\theta} & \Sigma_{\theta\varphi} \\ \Sigma_{\varphi\theta} & \Sigma_{\varphi\varphi} \end{pmatrix} = \begin{pmatrix} \left(\frac{\cos^2\xi}{\cos^2\chi} + \sin^2\xi\right)\Sigma_P & -\frac{\Sigma_H}{\cos\chi} + \frac{\sin^2\chi\sin\xi\cos\xi}{\cos^2\chi}\Sigma_P \\ \frac{\Sigma_H}{\cos\chi} + \frac{\sin^2\chi\sin\xi\cos\xi}{\cos^2\chi}\Sigma_P & \left(\frac{\sin^2\xi}{\cos^2\chi} + \sin^2\xi\right)\Sigma_P \end{pmatrix}, \qquad (7)$$

where χ is the angle between the magnetic field and the normal to the shell ionosphere and ξ is the angle between the vertical plane in which B stands and the meridian plane. Σ_P and Σ_H are the Pedersen and Hall conductances. Equations (6) and (7) are derived in Appendix A.

[18] The current density out of and into the ionosphere along magnetic field lines, namely, $\mathbf{j}_{//}$, is determined by the condition that the total current density remains divergence free, i.e., $\nabla\mathbf{j} = 0$:

$$\nabla \cdot \mathbf{J_H} = -j_{\|} \cos\chi \tag{8}$$

[*Vasyliunas*, 1970]. Combining shell Ohm's law (5) with the current continuity equation (8) and using $\mathbf{E} = -\nabla\mathbf{\Phi}$, Vasyliunas's equation becomes

$$\nabla \cdot [\Sigma(-\nabla\Phi) + \mathbf{J_w}] = -j_{\|} \cos\chi. \tag{9}$$

Because (6) and (7) are not defined along the magnetic dip equator, a Cowling current derived in Appendix A is used to model the current along the magnetic dip equator.

3.2. Coupling

[19] The conductivity parallel to **B** is so large that magnetic field lines are assumed equipotential:

$$\Phi_N(\alpha,\beta) = \Phi_S(\alpha,\beta), \tag{10}$$

where subcripts N and S stand for Northern and Southern Hemisphere footprints of the same field line.

[20] The magnetosphere is assumed empty, except Birkeland currents that are allowed to flow from one ionospheric hemisphere to the other one. There is then no current across the magnetic field and ($j_{//}/B$) is constant along a field line. Thus conjugated footprints satisfy

$$\left(\frac{j_{\|}}{B}\right)_S = \left(\frac{j_{\|}}{B}\right)_N. \tag{11}$$

Our assumptions (equipotential field lines, empty magnetosphere) transform the magnetosphere-ionosphere coupling to a Northern Hemisphere/Southern hemisphere coupling, illustrated by (10) and (11).

[21] Writing (9) for conjugated footprints and using (11), we get for each field line

$$\left(\frac{\nabla[\Sigma(-\nabla\Phi) + J_w]}{B\cos\chi}\right)_N = \left(\frac{\nabla[\Sigma(-\nabla\Phi) + J_w]}{B\cos\chi}\right)_S. \tag{12}$$

Under assumption of euipotential magnetic field line, i.e., $\Phi = \Phi(\alpha, \beta)$,

$$-\nabla\Phi\begin{pmatrix} -\frac{1}{R_e}\frac{\partial\Phi}{\partial\theta} \\ -\frac{1}{R_e\sin\theta}\frac{\partial\Phi}{\partial\varphi} \end{pmatrix} = \begin{pmatrix} -\frac{1}{R_e}\frac{\partial\Phi}{\partial\alpha}\frac{\partial\alpha}{\partial\theta} - \frac{1}{R_e}\frac{\partial\Phi}{\partial\beta}\frac{\partial\beta}{\partial\theta} \\ -\frac{1}{R_e\sin\theta}\frac{\partial\Phi}{\partial\alpha}\frac{\partial\alpha}{\partial\varphi} - \frac{1}{R_e\sin\theta}\frac{\partial\Phi}{\partial\beta}\frac{\partial\beta}{\partial\varphi} \end{pmatrix}. \tag{13}$$

Combining (10), (12), and (13) leads to the elliptical second-order differential equation for the ionosphere electrostatic potential:

$$P_1\frac{\partial^2\Phi}{\partial\alpha^2} + P_2\frac{\partial^2\Phi}{\partial\beta^2} + P_3\frac{\partial\Phi}{\partial\alpha} + P_4\frac{\partial\Phi}{\partial\beta} + P_5\frac{\partial^2\Phi}{\partial\alpha\partial\beta} = P_6, \tag{14}$$

where the P_i (i = 1,. . .,6) coefficients are derived in Appendix A and are obtained by subtraction of the south partial coefficients from the north ones ($P_1 = P_{1N} - P_{1S}$, etc.). The partial coefficients are given by

$$P_{1\,j=N,S} = \frac{1}{B\cos\chi}\left(-(A+C)\frac{\partial\alpha}{\partial\theta} - \frac{(G+I)}{\sin\theta}\frac{\partial\alpha}{\partial\varphi}\right)_{j=N,S}$$

$$P_{2\,j=N,S} = \frac{1}{B\cos\chi}\left(-(F+D)\frac{\partial\alpha}{\partial\theta} - \frac{(H+K)}{\sin\theta}\frac{\partial\alpha}{\partial\varphi}\right)_{j=N,S}$$

$$P_{3\,j=N,S} = \frac{1}{B\cos\chi}\left(-\frac{\partial(A+C)}{\partial\theta} - \frac{\cos\theta}{\sin\theta}(A+C) - \frac{1}{\sin\theta}\frac{\partial(G+I)}{\partial\varphi}\right)_{j=N,S}$$

$$P_{4\,j=N,S} = \frac{1}{B\cos\chi}\left(-\frac{\partial(F+D)}{\partial\theta} - \frac{\cos\theta}{\sin\theta}(F+D) - \frac{1}{\sin\theta}\frac{\partial(H+K)}{\partial\varphi}\right)_{j=N,S}$$

$$P_{5\,j=N,S} = \frac{-1}{B\cos\chi}\left((F+D)\frac{\partial\alpha}{\partial\theta} + (A+C)\frac{\partial\beta}{\partial\theta} + \frac{(G+I)}{\sin\theta}\frac{\partial\beta}{\partial\varphi} + \frac{(H+K)}{\sin\theta}\frac{\partial\alpha}{\partial\varphi}\right)_{j=N,S}$$

$$P_{6\,j=N,S} = \frac{-1}{B\cos\chi}\left(\frac{\partial J_{w\theta}}{\partial\theta} + \frac{\cos\theta}{\sin\theta}J_{w\theta} + \frac{1}{\sin\theta}\frac{\partial J_{w\varphi}}{\partial\varphi}\right)_{j=N,S},$$

where

$$J_{w\theta} = B\left(\frac{\cos^2\xi}{\cos\chi} + \sin^2\xi\cos\chi\right)\Sigma_P u_\varphi - B\left(\sin\xi\cos\chi\left(\frac{1}{\cos\chi} - \cos\chi\right)\Sigma_P - \Sigma_H\right)u_\theta$$

$$J_{w\varphi} = B\left(\sin\xi\cos\chi\left(\frac{1}{\cos\chi} - \cos\chi\right)\Sigma_P + \Sigma_H\right)u_\varphi - B\left(\frac{\sin^2\xi}{\cos\chi} + \cos^2\xi\cos\chi\right)\Sigma_P u_\theta$$

$$A = \left(\frac{\cos^2\xi}{\cos^2\chi} + \sin^2\xi\right)\frac{\Sigma_P}{R_E}\frac{\partial\alpha}{\partial\theta}$$

$$F = \left(\frac{\cos^2\xi}{\cos^2\chi} + \sin^2\xi\right)\frac{\Sigma_P}{R_E}\frac{\partial\beta}{\partial\theta}$$

$$C = \left(-\frac{\Sigma_H}{\cos\chi} + \frac{\sin^2\chi\sin\xi\cos\xi}{\cos^2\chi}\Sigma_P\right)\frac{1}{R_E\sin\theta}\frac{\partial\alpha}{\partial\varphi}$$

$$D = \left(-\frac{\Sigma_H}{\cos\chi} + \frac{\sin^2\chi\sin\xi\cos\xi}{\cos^2\chi}\Sigma_P\right)\frac{1}{R_E\sin\theta}\frac{\partial\beta}{\partial\varphi}$$

$$G = \left(\frac{\Sigma_H}{\cos\chi} + \frac{\sin^2\chi\sin\xi\cos\xi}{\cos^2\chi}\Sigma_P\right)\frac{1}{R_E}\frac{\partial\alpha}{\partial\theta}$$

$$H = \left(\frac{\Sigma_H}{\cos\chi} + \frac{\sin^2\chi\sin\xi\cos\xi}{\cos^2\chi}\Sigma_P\right)\frac{1}{R_E}\frac{\partial\beta}{\partial\theta}$$

$$I = \left(\frac{\sin^2\xi}{\cos^2\chi} + \cos^2\xi\right)\frac{\Sigma_P}{R_E\sin\theta}\frac{\partial\alpha}{\partial\varphi}$$

$$K = \left(\frac{\sin^2\xi}{\cos^2\chi} + \cos^2\xi\right)\frac{\Sigma_P}{R_E\sin\theta}\frac{\partial\beta}{\partial\varphi}.$$

3.3. Boundary Conditions and Numerical Considerations

[22] In order to solve the Poisson equation (14), two boundary conditions have to be imposed for the variable α: one at the magnetic equator and the other at the magnetic poles. Equation

(14) is not defined at the magnetic equator because field lines are tangential to the shell ionosphere ($\chi = 90°$). This propriety in fact allows for the derivation of a boundary condition [*Richmond*, 1995a]: No current can flow up from or down into the ionosphere at the magnetic equator. That is,

$$j_r = 0. \tag{15}$$

This condition is expressed in α, β coordinates (see Appendix A) as

$$L\frac{\partial\Phi\left(\alpha_{\text{equator}},\ \beta\right)}{\partial\alpha} + M\frac{\partial\Phi\left(\alpha_{\text{equator}},\ \beta\right)}{\partial\beta} = N, \tag{16}$$

where

$$L = -\sigma_P\frac{\partial\alpha}{\partial r} + \sigma_H\frac{B_\varphi}{|B|}\frac{1}{R_E}\frac{\partial\alpha}{\partial\theta} - \sigma_H\frac{B_\theta}{|B|}\frac{1}{R_E\sin\theta}\frac{\partial\alpha}{\partial\varphi}$$

$$M = -\sigma_P\frac{\partial\beta}{\partial r} + \sigma_H\frac{B_\varphi}{|B|}\frac{1}{R_E}\frac{\partial\beta}{\partial\theta} - \sigma_H\frac{B_\theta}{|B|}\frac{1}{R_E\sin\theta}\frac{\partial\beta}{\partial\varphi}$$

$$N = -\sigma_P\left(u_\theta B_\varphi - u_\varphi B_\theta\right).$$

[23] At the pole, equipotential field lines go to infinity where the electric potential is chosen to be zero as an ideal assumption:

$$\Phi(\alpha = 0) = 0 \tag{17}$$

In the β direction, the potential must feature a periodicity of 2π.

[24] Equations (14), (16), and (17) compose the system we solved numerically on the α-β grid. One hundred and one discrete values of α from 0 (corresponding with the magnetic pole) to 100 (corresponding with the magnetic equator) and 62 values of β from 0 to $2\pi + \pi/30$ (by step of $\pi/30$) are used. Near the magnetic equator and the pole, some quantities vary so fast that five intermediate α lines have been addedd between previous ones.

[25] Unavoidable errors in numerically calculating the coefficients of the linearized equation arise, and the numerical solution remains very sensitive to these coefficients. A constraint on the solution has been added to overcome this high sensitivity. It is based on the value of the shell current in the vicinity of the magnetic pole. The shell current flowing through the magnetic pole ($\alpha = 0$) is not calculated in our model and is logically set to zero. Physically, the shell current flowing across the $\alpha = 1$ line (the closest α line to the pole) should also be close to zero and is then used to constrain the solution of (14). It can be written as

$$I = \oint_{\alpha_1} \nabla\alpha \bullet J_H\ da, \tag{18}$$

where da is the increment along the $\alpha = 1$ line. The coefficient L in (16) is chosen to be slightly modified by a correction factor. This factor, the value of which is approximately one, is determined by dichotomy to ensure that I is zeroing. This method provides a correct simulated potential as it is shown in the mext section with the help of theoretical results in the case of dipole field under specific ionospheric conditions.

[26] Once this adjustment is completed and the suitable electric potential is determined, the electric field and the shell and Birkeland currents are readily calculated from $\boldsymbol{E} = -\nabla\Phi$ and (5) and (8), respectively.

4. Validation: Case of Uniform Conductances and Rotational Wind

[27] Equation (14), subject to the boundary conditions (16) and (17), is linearized on a 101 × 62 grid. The system of 6262 linear algebraic equations is solved by Gaussian elimination. The results presented here are obtained by setting uniform conductances ($\Sigma_P = \Sigma_H = 1$ S). The neutral wind is purely zonal (no vertical or meridional wind) and satisfies

$$u_\varphi = C\sin\theta, \tag{19}$$

where θ is the geographic colatitude and hence the constant C is the neutral velocity at the geographical equator. C value is fixed to 100 m s^{-1}. For comparison, the amplitude of the zonal neutral wind fluctuates in the range [−100 to +200 m s^{-1}], providing a daily average superrotation of the neutral ionosphere of about 10 m s^{-1} at equatorial latitudes [*Herrero and Mayr*, 1986]. Notice that our zonal wind is consistent with this superrotation of the ionosphere, which is the first order of the zonal neutral wind represented as a Fourier series expansion [*Herrero and Mayr*, 1986] and which has been shown to decrease with latitude according to satellite observations [*Maynard et al.*, 1988; *Coley and Heelis*, 1989]. Although uniform conductances prevent any comparison with observations, a theoretical solution of (14) can be derived in the dipole case under these conditions and makes it possible to test our computer code.

[28] In a dipolar magnetic field, α and β can be defined by

$$\alpha = -\frac{B_0 R_E^3 \sin^2\theta}{r} \tag{20a}$$

$$\beta = \varphi, \tag{20b}$$

where B_0 (30,200 nT) is the magnitude of the field on Earth's surface in the magnetic equatorial plane. The magnetic field satisfies

$$B = B_0\sqrt{4 - 3\sin^2\theta} \tag{21}$$

$$\cos\chi = \frac{-\cos\theta}{\sqrt{1 - 0.75\sin\theta}}. \tag{22}$$

Under the assumptions of uniform and equal conductances, and with respect to the neutral wind defined by (19), the P_i coefficients of equation (14) can be formally derived and the electric potential

$$\Phi_{\text{sol}} = -R_E B_0 C\sin^2\theta = \alpha C/R_E \tag{23}$$

is proved to be a solution of (14) and hence proportional to α and independent of β. Because geographic and magnetic hemispheres are exactly alike in a dipole field, all of the meridians feature the same electric potential distribution. A longitudinally uniform and strictly latitudinal electric polarization field results from this potential that produces no current, as for any steady zonal wind featuring no altitude variations along integrals path [*Richmond et al.*, 1976].

[29] Numerical errors due to linearization on a grid appear twice in the resolution of (14). First, because they depend on partial derivatives of α and β, the computation of the P_i coefficients is a source of error. Second, the resolution itself provides an approximate solution, because of the linearization. To investigate these sources of error, (14) is solved twice, once with numerical coefficients and once with theoretical ones. Both numerical potential results are then compared with the theoretical potential given by (23).

[30] Figure 2 presents four different electric potentials along one meridian. The semitheoretical potential is defined as the one obtained by solving (14) numerically, in which theoretical coef-

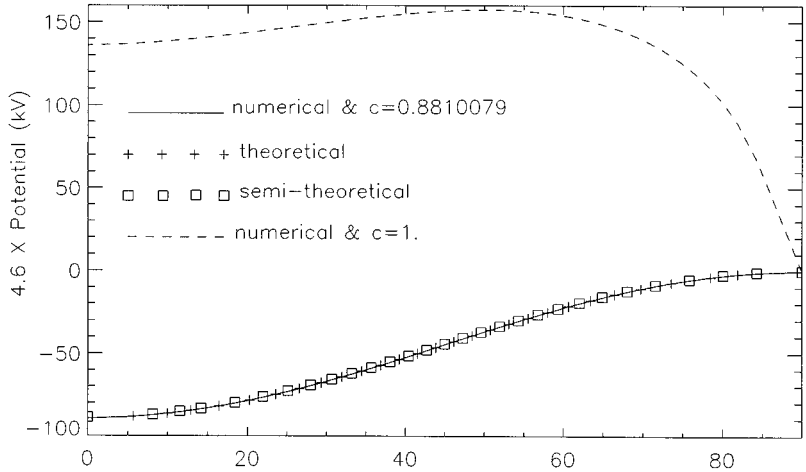

Figure 2. Numerical, semitheoretical, and theoretical electric potential distributions along one meridian in the Northern Hemisphere in a dipole field. Variable c is the correction factor used.

ficients are used. It is seen that it is very close to the theoretical potential, proving that our α-β grid sizes are suitable to reproduce the electric potential. Two numerical solutions (i.e., solved with numerical P_i) are also plotted. The first one is obtained without any correction and features a very large departure from the theoretical potential, meaning that the computation of P_i coefficients with our grid is not accurate enough to imply a good resolution. In other words, the sensitivity of the equation to its coefficients is very high. This is confirmed by the error found between theoretical and numerical P_i, which reaches a few percent for some coefficient in the vicinity of the magnetic equator. This conclusion leads to the introduction of the correction factor defined in section 3. The second numerical potential in Figure 2 is obtained with a correction factor of 0.8810079 ± 5.10^{-7} that ensures that no current flows toward the pole and provides eventually a good solution. Thus the resolution itself induces negligible error, and the main error comes from the P_i coefficient computation that is overcome with a constraint on current.

[31] Once the electric potential is calculated, computation of electric fields, currents, and drift velocity is the second phase of the procedure. The relevant quantity is then not the electric potential but its derivatives. Errors arising during this second step are examined directly through simulated currents.

[32] Simulations with a tilted dipole and IGRF provide current amplitude larger by 1–3 orders of magnitude than with dipole. This confirms that the current density is negligible in the dipole case. However, it is not exactly zeroing as expected. Figure 3 shows the maximum absolute value of its shell components (J_θ and J_φ) and of the Birkeland current density found at each latitude. It is seen that the use of computed derivatives leads to inexact results around the magnetic dip equator (two α lines) but not at the magnetic dip equator itself. Notice that the vicinity of the magnetic equator is also the region where our physical assumption of a constant dip angle along a field line is invalid. Electric current results are considered reliable outside this area, with incertitude of ±0.2 mA m^{-1}. As for Birkeland current, an error of $\pm 5 \times 10^{-11}$ A m^{-2} is found.

[33] Finally, our code is valid to derive the electric potential at all latitudes and to derive other electrodynamic quantities at all magnetic latitudes, save the four α lines around the magnetic equator. Where they are reliable, Birkeland and shell currents are defined with $\pm 0.5 \times 10^{-10}$ A m^{-2} and ±0.2 mA m^{-1}, respectively. Aware of these limitations, we can use the dynamo code to experiment with the effects of magnetic models. Because simulation results undergo important changes when conductivity and neutral wind distributions change, simulations are performed with realistic ionospheric distributions and presented in the next section.

5. Application: Case of Simple Tidal Wind and Conductances

[34] Simulation results are obviously sensitive to the wind and conductance distributions and to the magnetic field configuration. In this section, symmetric wind and conductance distributions under equinox conditions are used. They are acceptable in the sense that they permit us to reproduce general features of the dynamo system, and they allow us to concentrate on asymmetric effects of the magnetic field configuration.

[35] For our modest goal, we follow *Heelis et al.* [1974] and *Farley et al.* [1986] to define the neutral wind and conductance distributions. The ionosphere is represented by a thin E layer and the F layer is neglected. For our simple two-dimensional E region model, integrated Pedersen and Hall conductivities are assumed proportional to the maximum electron density N_m multiplied by $1.2 \times 10^{-10}$and 2×10^{-10}, respectively, in SI units. For the daytime densities we assume

$$N_m = 1.4 \times 10^{11}[(1 + 0.008\ R_Z)\ \cos\psi]^{1/2}\left[m^{-3}\right], \qquad (24)$$

where R_z is the sunspot number, set to 50 in the following results, and ψ is the solar zenith angle. The nighttime N_m is taken to be constant and equal to 5×10^9 m^{-3}. The E region tidal wind is obtained from studies of solar tides in the dynamo region made by *Tarpley* [1970]. The fundamental evanescent (1, −2) solar diurnal mode, in which the southward and eastward winds are proportional to sin (ϕ + ϕ_0) and sin (ϕ + ϕ_0 + 90°), respectively, is chosen. The phase ϕ_0, which is typically somewhere near 270°, is taken equal to 250°. This phase value best fits observations [*Farley et al.*, 1986], and the wind is defined as follows:

$$u_\theta = 130\, f_1(\theta)\sin(\phi + 250^\circ)\ \ \mathrm{m\ s^{-1}} \qquad (25a)$$

$$u_\phi = 130\, f_2(\theta)\sin(\phi + 340^\circ)\ \ \mathrm{m\ s^{-1}} \qquad (25b)$$

The functions f_1 and f_2 represent the latitudinal dependence and are given by rather complicated Hough function expressions.

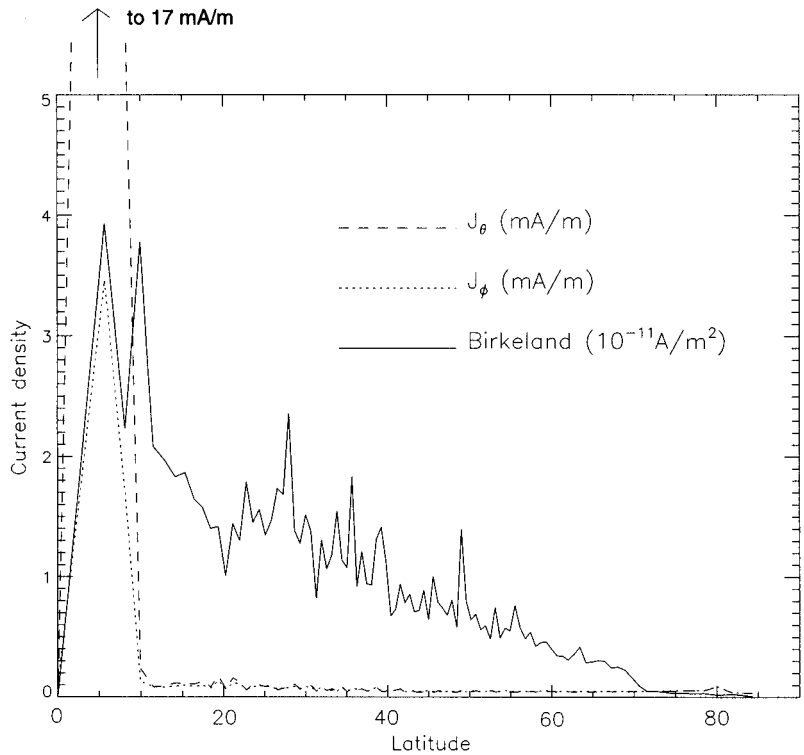

Figure 3. Maximum of absolute shell current components (J_θ, J_φ) and Birkeland current density found at each latitude in the Northern Hemisphere in a dipole field.

For our purpose, the following approximations, extracted from *Heelis et al.* [1974], are used:

$$f_1(\theta) = 2\ \theta/\pi - 1 \tag{26a}$$

$$f_2(\theta) = 3\ \theta/\pi - 1 \qquad 0 < \theta < \pi/3 \tag{26b}$$

$$f_2(\theta) = 1.2\ \theta/\pi - 0.4 \qquad \pi/3 < \theta < \pi/2 \tag{26c}$$

$$f_2(\theta) = -1.2\ \theta/\pi - 0.8 \qquad \pi/2 < \theta < 2\pi/3 \tag{26d}$$

$$f_2(\theta) = -3\ \theta/\pi + 2 \qquad 2\pi/3 < \theta < \pi, \tag{26e}$$

where θ is still the colatitude.

[36] Important limits to modeling dynamo processes follow from this ionospheric model. By neglecting the *F* region, the preversal enhancement of the zonal electric field cannot be explained [*Farley et al.*, 1986]. The *F* region dynamo is also considered as important as the *E* region dynamo at all local time at low latitudes [*Crain et al.*, 1993] and for nightime features [e.g., *Richmond*, 1989], particularly in the 1900–2100 LT region [*Maynard et al.*, 1995] As for the fundamental diurnal tidal wind, it is considered as the main contributor to the dynamo and is capable of accounting for most of the *Sq* current [*Richmond et al.*, 1976], although other tides are important in explaining the observed electric fields [*Richmond*, 1995b]. Neglecting electric fields that originate in the magnetosphere–solar wind interaction region and that map to the high-latitude ionosphere prevents us from reproducing the high-latitude characteristics. Note also that a penetration of these electric fields to low latitudes is still open for further discussions for nighttime conditions [*Wagner et al.*, 1980]. However, reasonable conclusions about the importance of the magnetic field configuration for dynamo large-scale processes can be drawn by using this ionospheric model.

5.1. Electrostatic Potential

[37] Figure 4 presents the electrostatic potential for three magnetic field configurations: dipole (DP), tilted dipole (TD), and IGRF. The bold dotted lines represents the magnetic dip equator. All three cases feature a maximum at equatorial dawn and a minimum at equatorial postdusk, as shown by previous models [e.g., *Takeda*, 1990]. When departures of the magnetic field from dipolar configuration are taken into account, the symmetry with respect to the magnetic equator in α-β coordinates is disorted and disappears in geographic coordinates, but, on a global scale, geometric characteristics of the potential are similar with the three fields.

[38] Some differences, however, are noticeable. For example, the potential difference between dusk and dawn at equator is about 14.9, 16.5, and 14.8 kV for DP, TD, and IGRF cases, respectively. These values are higher than those obtained from previous simulations: Typical values have usually been found around 5 kV [e.g., *Richmond et al.*, 1980, 1992; *Takeda et al.*, 1986; *Takeda and Maeda*, 1980] or 10 kV [*Heelis et al.*, 1974; *Crain et al.*, 1993]. This discrepancy in the electrostatic potential variation mainly comes from neglecting the *F* region and from the conductance model. Nevertheless, when compared with IGRF results, the potential difference is correct in DP case and overestimated in TD cases. Another illustration of the potential modulation induced by nondipolar components of the magnetic field is found in the morning sector. In the three cases, the maximum at equatorial dawn is relative and the absolute maximum, indicated by diamonds in Figure 4, is localized at midlatitude dawn. This characteristic has already been simulated [*Heelis et al.*, 1974; *Crain et al.*, 1993; *Takeda and Maeda*, 1980], and the resulting latitudinal gradient at dawn is steeper in DP cases: In the morning, the

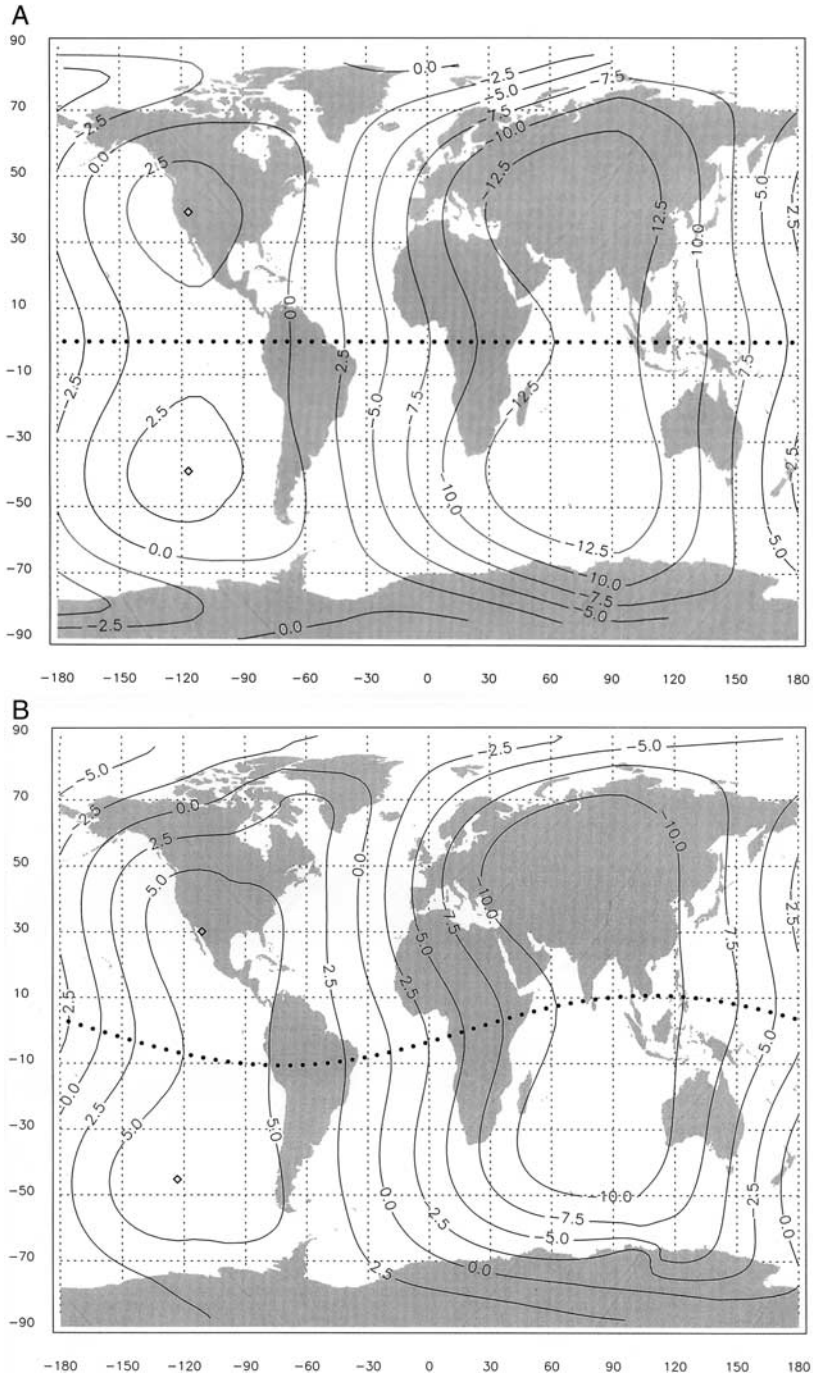

Figure 4. Contours of ionospheric electric potential (in kilovolts) driven by a diurnal tidal wind (a) in a dipole field, (b) in a tilted dipole field, and (c) in the IGRF 1995. Diamonds indicate potential maxima. Contours are drawn each 2.5 kV.

potential differences between midlatitudes and magnetic equator maxima are about 1.7, 1.2, and 1.5 kV in DP, TD, and IGRF cases, respectively. Here the DP simulation overestimates and the TD simulation underestimates the potential latitudinal gradient produced with IGRF, while the situation is roughly opposite in case of the equator dawn-dusk gradient in the previous example. It also turns out that DP estimations are slightly better than TD ones. These changes in the potential gradients certainly depend on UT and are finally not dramatic, but they have noticeable effects on the calculated electric currents.

5.2. Shell Currents

[39] Our simulation results are shown in Figure 5. They reproduce two daytime vortices observed on *Sq* current distributions, one anticlockwise in the Northern Hemisphere and the other clockwise in the Southern Hemisphere, and the boundary between the two vortices follows the geomagnetic equator. Vortex foci, localization of which depends on the hemisphere, on the season, and on UT, are found in a 30°–40° latitude range, which is the mean range observed for *Sq* current foci [*Wagner et al.*, 1980]. The maximum current

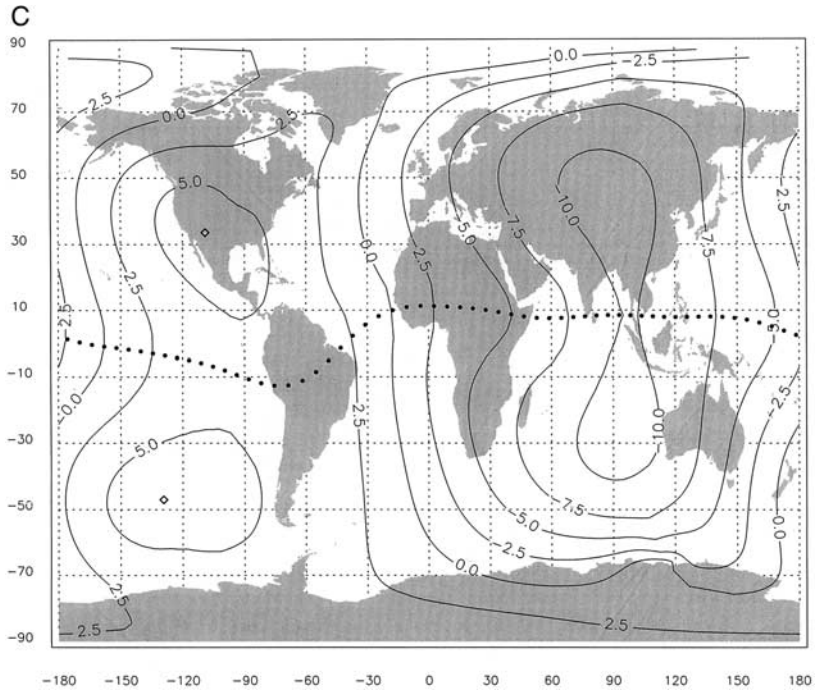

Figure 4. (continued)

densities at midlatitudes are about 70, 60, and 60 A km^{-1} in DP, TD, and IGRF, respectively. In the vicinity of the magnetic equator, these maxima become 96, 116, and 101 A km^{-1}. Keeping in mind that there is not strict equivalence between *Sq* current and horizontal integrated ionospheric current, these values are nonetheless of the same order of magnitude as the observed *Sq*current density: 20–50 A km^{-1} at midlatitudes and 100–200 A km^{-1} near geomagnetic equator [*Wagner et al.*, 1980].

[40] Even if these general attributes are well reproduced with the three magnetic field configurations, direction and magnitude of the currents are quite modified by the nondipolar distortions of the magnetic field. In fact, some dynamo characteristics can be simulated only if IGRF is used. In particular, there is a characteristic noticed in equivalent current system that has not yet received satisfactory explanation. This is the time lag between the foci of both hemisphere at equinox, which has been observed at all UT with an average value of about 1 hour [*Malin and Gupta*, 1977; *Wagner et al.*, 1980]. In Figure 5, currents simulated with IGRF only display this time lag, with the south focus in the afternoon leading the north focus by a few hours. A previous attempt to simulate the equinoctial time lag exists: *Stening* [1971] uses the symmetric tidal wind defined in the present paper and modulates the conductances and the dynamo emf $\mathbf{u} \times \mathbf{B}$ by using IGRF 1965 to introduce asymmetry in the dynamo. It has to be noticed that the longitudinal step of his model grid is 15°, i.e., 1 hour, which limits the local time accuracy of the results. A time shift of about 2 hours is seen in the Europe/Africa sector, but no time shift is seen in the American and Asian sectors. The inability to generate a 1-hour averaged time lag is likely due to the method used to connect hemispheres: They are linked geographically, i.e., as if the field were dipolar, and not through realistic magnetic field lines, like in our model. To confirm this idea, we have performed simulations for each hour of UT. The UT variation of the local time difference of the current foci in both hemispheres is shown in Figure 6. The shape of the curve is remarkably similar to the one deduced from observations for *Sq*equivalent current [*Wagner et al.*, 1980, Figure 7], with a maximum around 1000–1200 UT and a minimum when noon is above the Pacific (2000–2400 UT). This feature shows the importance of interhemispheric coupling along real field lines to explain the *Sq* foci time lag. Altough horizontal currents are considered, a 62-min averaged local time difference is obtained, in agreement with the 73 ± 21 min observed in *Sq* system [*Malin and Gupta*, 1977]. However, when it is positive, the simulated time lag is larger than the one featured by *Sq* current, and the minimum values are negative while they are still positive for observed *Sq*. These discrepancies may be attributed to the difference between *Sq* and horizontal currents, although it is not clear how considering *Sq* instead of horizontal current would modify the simulation results. It is then concluded that an equinox time lag featuring UT variations similar to those observed in *Sq* system can be simulated if parallel currents are allowed to flow along realistic field lines.

5.3. Birkeland Current

[41] We show distributions of Birkeland current for TD and IGRF cases in Figure 7, where the nonrealistic high-latitude and equatorial results are not displayed for clarity. With the adopt convention, positive currents flow out of the ionosphere and negative currents flow into the ionosphere. For a better rendition, hatched areas and dotted lines indicate the regions where currents flow out of and into the ionosphere, respectively. The contour levels have been chosen to emphasize the daytime structure.

[42] Field-aligned currents are caused by asymmetry in the distributions. When a dipole is used, there is no asymmetry in our model and no parallel current. However, some residual currents are present in the DP case simulation. They are between 0 and 1.2 $\times$ 10^{-10} A m^{-2}, 1–2 orders of magnitude less than TD and IGRF cases. This value is then used to specify the numerical error of our computations and show that nighttime features in Figure 7 are not reliable. In Figure 7 the magnetic field asymmetry is only source of Birkeland currents, the amplitudes of which are found between 0 and 1.3 $\times$ 10^{-8} A m^{-2} at midlatitudes. This estimation is identical to those obtained by previous models of asymmetric dynamo [*Maeda*, 1974; *Stening*, 1977; *Richmond and Roble*, 1987; *Takeda*, 1982, 1990]. For

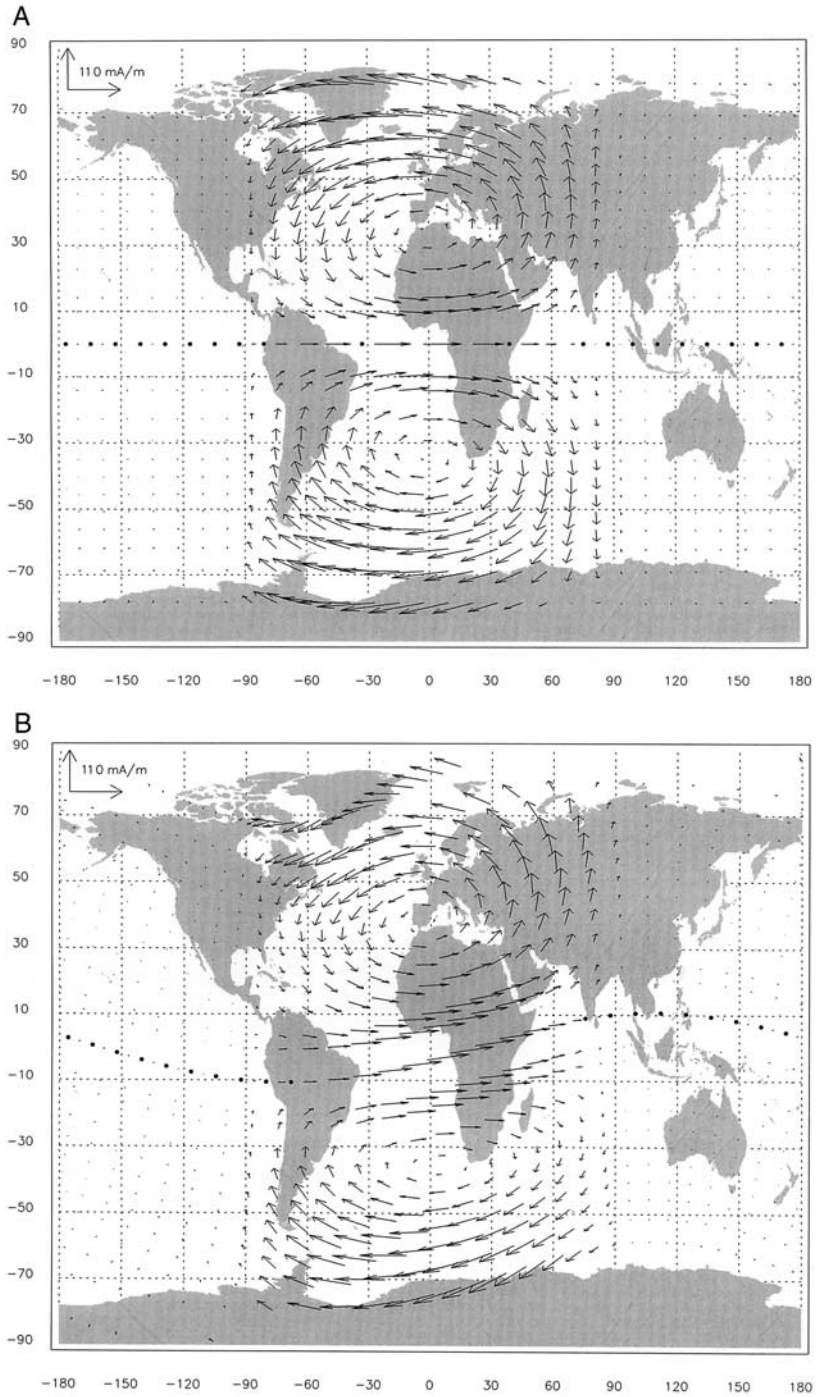

Figure 5. Ionospheric shell currents (a) in a dipole field, (b) in a tilted dipole field, and (c) in the IGRF 1995.

now, the different assumptions used in the models, as well as the lack of observations, limit the comparison to order of magnitude, and it is finally concluded that the magnetic field asymmetry is as efficient as the conductivity and neutral wind asymmetries used in previous models in driving Birkeland currents.

[43] The importance of the magnetic field configuration to determine the pattern of field-aligned current is also confirmed. First, the TD patterns derived by *Richmond and Roble* [1987] for 1100 UT at equinox and *Takeda* [1982] for 1200 UT are similar to Figure 7a. Because this similarity is obtained with different wind and conductance distributions, it emphasizes the role of the magnetic field. Second, these TD patterns differ from the one featured in Figure 7b for the IGRF case, mainly at midlatitudes between 1000 and 1400 LT, where the dynamo models are usually the most reliable. The magnetic field asymmetry eventually turns out to be as important as wind and conductance asymmetries, not only to drive Birkeland current but also to specify their pattern.

6. Conclusions

[44] A computer code based on Euler potentials coordinates has been developed for the ionospheric dynamo. The coordinate system is aligned with the geomagnetic field, which is adequately represented by the Earth's main field alone in conditions of magnetic quiescence and has been built for three magnetic field configura-

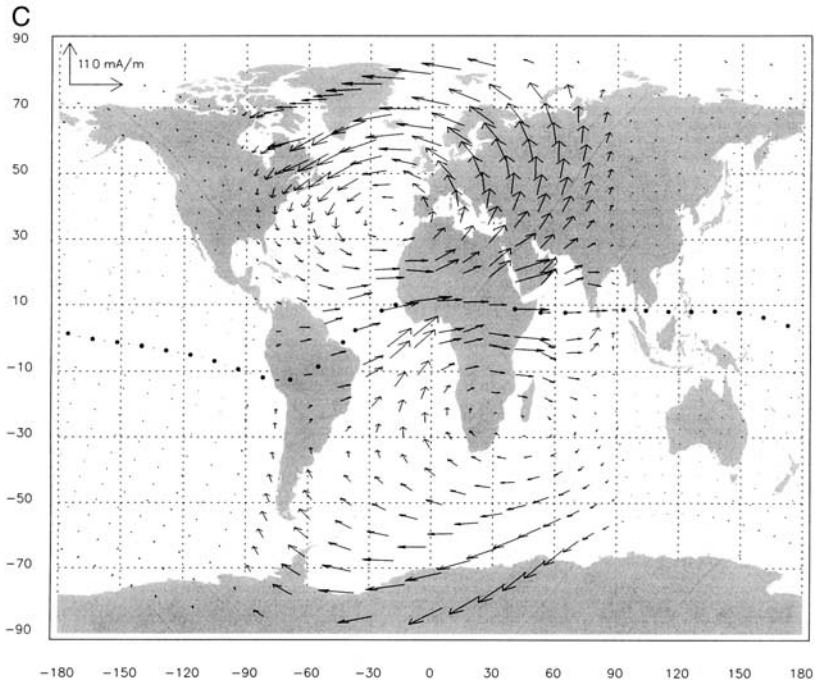

Figure 5. (continued)

tions: dipole, tilted dipole, and IGRF. By using a simple zonal neutral wind and uniform conductances, for which a theoretical solution for electric potential and ionospheric currents exists in case of a dipolar field, some limits of our model have been determined. At the present state of development, the electric potential is correctly solved at all latitudes, but horizontal and parallel currents are roughly estimated in the vicinity of the magnetic dip equator. The nighttime and high-latitude ionospheres are not realistic.

[45] To analyze the influence of magnetic configuration on simulation results, more realistic distributions of conductivity and neutral wind have been used. At equinox, they are asymmetric with respect to the geographic equator, which isolates asymmetric effects of the sole magnetic field. The realistic characteristic allows for the reproduction of the main features of the dynamo system: general geometry of the electrostatic potential, current vortices, and shell current and Birkeland current magnitudes. The main conclusions drawn from the simulations are as follows:

1. Departures of the geomagnetic field from dipolar configuration induce slight modulations of the electrostatic potential but important variations in current strength and direction, as illustrated by the geographic position of the horizontal current foci and field-aligned current pattern,

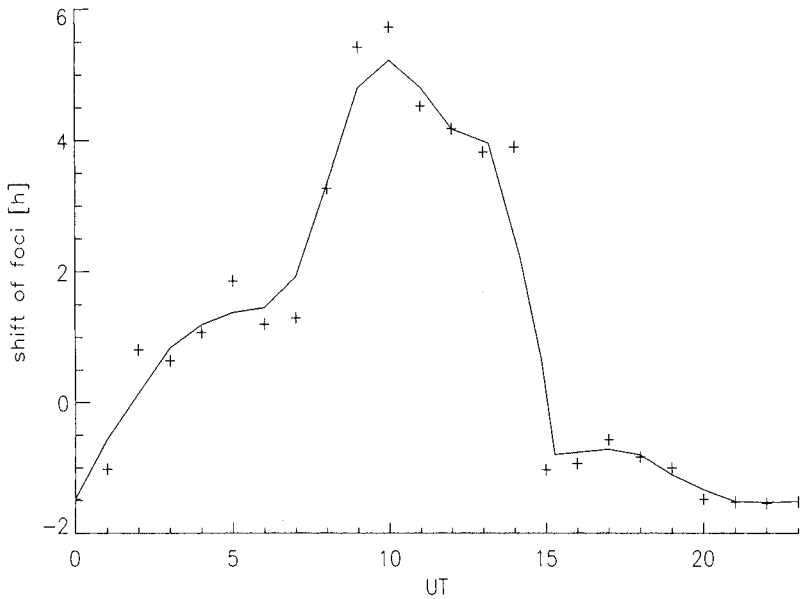

Figure 6. Universal time variation of the local time difference of the horizontal current foci.

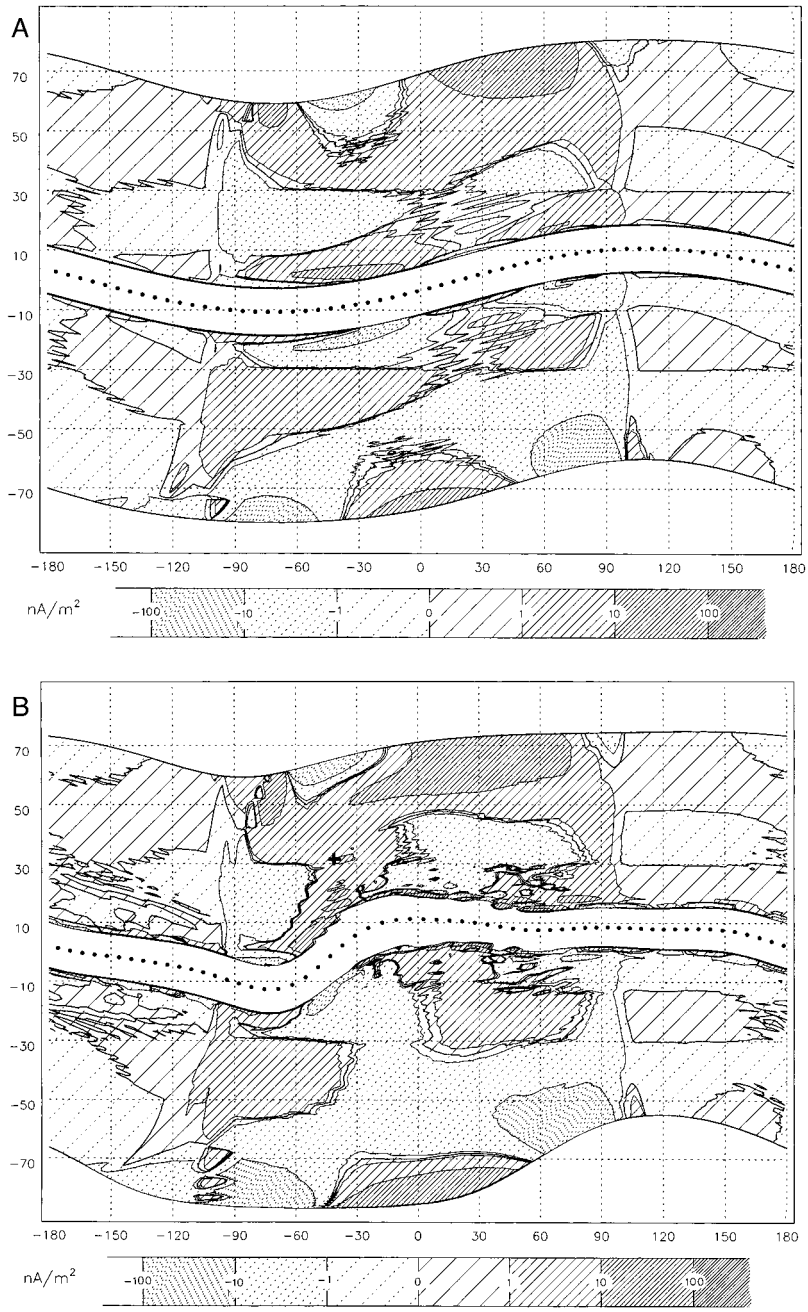

Figure 7. Birkeland currents driven by magnetic field asymmetry in the case of (a) tilted dipole and (b) IGRF 1995. Contours are drawn at ±0, 10^0, 10^1, and 10^2 nA m^{-2}. Positive currents flow out of the ionosphere, and are represented by hatched regions that are closer to each other for higher values. The cross in Figure 7b stands for a local maximum of 1.3×10^{-12}A cm^{-2}.

2. It has been noticed that including the tilt of the dipole is a poor improvement of the dipolar approximation. Although Birkeland currents are generated under TD configuration, their pattern differs from the IGRF pattern, and horizontal currents differ from IGRF currents as much as DP currents do. Typically, the local time lag between the horizontal current foci is not produced under TD and DP configurations,

3. A foci local timelag in horizontal current at different UT for equinox has been reproduced with IGRF. It is attributed to the possibility of parallel current flowing along realistic field lines and is obviously related to the foci local time difference observed at equinox at all UT in *Sq* current,

4. The asymmetry of the magnetic field drives field-aligned current of the same order of magnitude as wind and conductance asymmetries used in previous dynamo models. Since the interhemispheric coupling occurs along field lines, it also significantly specifies the pattern of Birkeland current, which is provided here for the first time for the realistic IGRF. Note that the modulation of conductivity by the field, which is another important source of asymmetry [*Stening*, 1977], is not included in the model.

[46] In summary, our results suggest that the thermosphere-ionosphere-magnetosphere system is significantly affected by departures of the geomagnetic field from dipolar configuration,

as already shown for the thermosphere-ionosphere coupling by *Richmond et al.* [1992]. In particular, the coupling along realistic field lines is expected to shed light on UT variations of the current system that have not yet been successfully simulated, like the phase behavior of the total current in both hemispheres [*Wagner et al.*, 1980]. Comprehensive UT studies will be provided in future papers.

Appendix A

[47] Vectors $\mathbf{e}_r$, $\mathbf{e}_\theta$, $\mathbf{e}_\varphi$ are the unit vectors associated with the spherical coordinates, and all other notations are those previously defined in the text.

A1. Derivation of the Differential Equation

[48] The electric current (equation (4)) is separated in two parts due to the electric field and the neutral wind:

$$j = [\sigma]\mathbf{E} + \mathbf{j}_w, \tag{A1}$$

where $[\sigma]$ is the conductivity tensor. First, the wind part is neglected and the magnetic field is taken in the meridian plane (i.e., $\xi = 0$). Following *Baker and Martyn* [1953], E_r is solved by imposing $j_r = 0$. For the two other current components, we put $\sigma_0$to the limit of infinity, leading in the coordinates system (θ, φ) to

$$[\sigma] = \begin{pmatrix} \sigma_{\theta\theta} & \sigma_{\theta\varphi} \\ \sigma_{\varphi\theta} & \sigma_{\varphi\varphi} \end{pmatrix} = \begin{pmatrix} \frac{\sigma_P}{\cos^2\chi} & -\frac{\sigma_H}{\cos\chi} \\ \frac{\sigma_H}{\cos\chi} & \sigma_P \end{pmatrix}. \tag{A2}$$

[49] This conductivity tensor is then integrated along the field line to give the conductance tensor, where conductances are defined by $\Sigma_p = \int \sigma_p dl$ and $\Sigma_H = \int \sigma_H dl$. The conductance tensor (equation (7)) in the general case (i.e., $\xi \neq 0$) is obtained by a rotation transformation of ξ about the r axis ($\boldsymbol{e}_\theta$ is replaced by $\cos\xi\ \boldsymbol{e}_\theta + \sin\xi\ \boldsymbol{e}_\varphi$ and e_φ is replaced by $-\sin\xi\ \boldsymbol{e}_\theta + \cos\xi\ \boldsymbol{e}_\varphi$).

[50] The part of the shell current due to neutral wind,

$$\mathbf{j}_w = \sigma_P(\mathbf{u}\times\mathbf{B})_\perp + \sigma_H\ \mathbf{b}\times(\mathbf{u}\times\mathbf{B}), \tag{A3}$$

becomes, if the magnetic field is in the meridian plane,

$$j_w = B\left[\sigma_H \mathrm{u}_\theta + \frac{\sigma_P \mathrm{u}_\varphi}{\cos\chi}\right]\mathbf{e}_\theta + B\left[-\cos\chi\,\sigma_P \mathrm{u}_\theta + \sigma_H \mathrm{u}_\varphi\right]\mathbf{e}_\varphi. \tag{A4}$$

After rotation transformation of angle ξ about the $r$axis ($\mathbf{u}_\theta$ is replaced by $\cos\xi\ \mathbf{u}_\theta + \sin\xi\ \mathbf{u}_\varphi$ and $\mathbf{u}_\varphi$ is replaced by $-\sin\xi\ \mathbf{u}_\theta + \cos\xi\ \mathbf{u}_\varphi$), components of $\boldsymbol{j}_w$ are

$$\begin{cases} J_{w\theta} = B\left(\frac{\cos^2\xi}{\cos\chi} + \sin^2\xi\cos\chi\right)\sigma_P u_\varphi - B\left(\sin\xi\cos\chi\left(\frac{1}{\cos\chi} - \cos\chi\right)\sigma_P u_\theta - \sigma_H u_\theta\right) \\ J_{w\varphi} = B\left(\sin\xi\cos\chi\left(\frac{1}{\cos\chi} - \cos\chi\right)\sigma_P u_\varphi + \sigma_H u_\varphi\right) - B\left(\frac{\sin^2\xi}{\cos\chi} + \cos^2\xi\cos\chi\right)\sigma_P u_\theta. \end{cases} \tag{A5}$$

Field line integration of (A5) then leads to (6).

[51] Combining (13) with (5), (6), and (7)results in the total shell current expression

$$\begin{cases} J_\theta = -\frac{\Sigma_{\theta\theta}}{R_E}\frac{\partial\Phi}{\partial\alpha}\frac{\partial\alpha}{\partial\theta} - \frac{\Sigma_{\theta\theta}}{R_E}\frac{\partial\Phi}{\partial\beta}\frac{\partial\beta}{\partial\theta} - \frac{\Sigma_{\theta\varphi}}{R_E\sin\theta}\frac{\partial\Phi}{\partial\alpha}\frac{\partial\alpha}{\partial\theta} - \frac{\Sigma_{\theta\varphi}}{R_E\sin\theta}\frac{\partial\Phi}{\partial\beta}\frac{\partial\beta}{\partial\theta} + J_{w\theta} \\ J_\varphi = -\frac{\Sigma_{\varphi\theta}}{R_E}\frac{\partial\Phi}{\partial\alpha}\frac{\partial\alpha}{\partial\varphi} - \frac{\Sigma_{\varphi\theta}}{R_E}\frac{\partial\Phi}{\partial\beta}\frac{\partial\beta}{\partial\varphi} - \frac{\Sigma_{\varphi\varphi}}{R_E\sin\theta}\frac{\partial\Phi}{\partial\alpha}\frac{\partial\alpha}{\partial\varphi} - \frac{\Sigma_{\varphi\varphi}}{R_E\sin\theta}\frac{\partial\Phi}{\partial\beta}\frac{\partial\beta}{\partial\varphi} + J_{w\varphi}, \end{cases} \tag{A6}$$

which is (5) expressed in (θ, φ) coordinates. Finally, using (A6) in (12) leads to the Poisson's equation (14) where $P_i (i = 1\ldots6)$ are readily calculated.

[52] Note that to get (6) and (7), wind components, elctric field B, and angles χ and ξ are assumed constant along the field lines in the conducting layer, where integrations are performed.

A2. Derivation of the Boundary Condition Equation

[53] Equation (17) can be written as $\boldsymbol{j}\cdot\mathbf{e}_r = 0$, that is, using Ohm's law (equation (4)):

$$\begin{aligned} &-\sigma_P\frac{\partial\Phi}{\partial\alpha}\nabla\alpha\cdot\mathbf{e}_r - \sigma_P\frac{\partial\Phi}{\partial\beta}\nabla\beta\cdot\mathbf{e}_r + \sigma_H\frac{B_\varphi}{|B|}\frac{\partial\Phi}{\partial\alpha}\nabla\alpha\cdot\mathbf{e}_\theta + \sigma_H\frac{B_\varphi}{|B|}\frac{\partial\Phi}{\partial\beta}\nabla\beta\cdot\mathbf{e}_\theta \\ &-\sigma_H\frac{B_\theta}{|B|}\frac{\partial\Phi}{\partial\alpha}\nabla\alpha\cdot\mathbf{e}_\varphi - \sigma_H\frac{B_\theta}{|B|}\frac{\partial\Phi}{\partial\beta}\frac{\partial\beta}{\partial\varphi}\nabla\beta\cdot\mathbf{e}_\varphi - \sigma_P\left(u_\theta B_\varphi - u_\varphi B_\theta\right) = 0 \end{aligned} \tag{A7}$$

Derivations of the boundary conditon coefficients, *L, M,* and *N*, are straightforward.

A3. Generalized Cowling Current

[54] Equation (4) is written

$$\begin{cases} j_r = \overbrace{\sigma_P\left(E_r + u_\theta B_\varphi - u_\varphi B_\theta\right)}^{E_{PO}} + \overbrace{\frac{\sigma_H}{|B|}\left(E_\varphi B_\theta - E_\theta B_\varphi\right)}^{\text{Hall vertical field}} \\ j_\theta = \sigma_P E_\theta + \frac{\sigma_H}{|B|}B_\varphi\left(E_r + u_\theta B_\varphi - u_\varphi B_\theta\right) \\ j_\varphi = \sigma_P E_\varphi - \frac{\sigma_H}{|B|}B_\theta\left(E_r + u_\theta B_\varphi - u_\varphi B_\theta\right). \end{cases} \tag{A8}$$

According to the boundary condition (15),

$$E_{PO} \equiv \left(E_r + u_\theta B_\varphi - u_\varphi B_\theta\right) = -\frac{\sigma_H}{\sigma_P}\frac{1}{|B|}\left(E_\varphi B_\theta - E_\theta B_\varphi\right) \tag{A9}$$

is a vertical polarization field that compensates the Hall vertical field (right member), so that finally no vertical current flows. This field drives a horizontal Hall current, which adds to the primary Pedersen current

$$\begin{cases} j_\theta = \sigma_P E_\theta - \frac{\sigma_H^2}{\sigma_P}\frac{B_\varphi}{|B|^2}\left(E_\varphi B_\theta - E_\theta B_\varphi\right) \\ j_\varphi = \sigma_P E_\varphi + \frac{\sigma_H^2}{\sigma_P}\frac{B_\theta}{|B|^2}\left(E_\varphi B_\theta - E_\theta B_\varphi\right). \end{cases} \tag{A10}$$

Equation (A10) expresses the Cowling conductivity in spherical coordinates.

[55] **Acknowledgments.** The authors are grateful to Dick Wolf for valuable discussions. This work was supported by NSF grant ATM-0095013.

[56] Janet G. Luhmann thanks the referees for their assistance in evaluating this paper.

References

Baker, W. G., and D. F. Martyn, Electric currents in the ionosphere, I, The conductivity, *Philos. Trans. R. Soc. London, Ser. A*, *246*, 281–294, 1953.

Coley, W. R., and R. A. Heelis, Low-latitude zonal and vertical ion drifts seen by DE 2, *J. Geophys. Res.*, *94*, 6751–6761, 1989.

Coley, W. R., J. P. McClure, and W. B. Hanson, Equatorial fountain effect and dynamo drift signatures from AE-E observations, *J. Geophys. Res.*, *95*, 21,285–21,290, 1990.

Crain, D. J., R. A. Heelis, G. J. Bailey, and A. D. Richmond, Low-latitude plasma drifts from a simulation of the global atmospheric dynamo, *J. Geophys. Res.*, *98*, 6039–6046, 1993.

Eccles, J. V., Modeling investigation of the evening prereversal enhancement of the zonal electric field in the equatorial ionosphere, *J. Geophys. Res.*, *103*, 26,709–26,719, 1998.

Farley, D. T., E. Bonelli, B. G. Fejer, and M. F. Larsen, The prereversal enhancement of the zonal electric field in the equatorial ionosphere, *J. Geophys. Res.*, *91*, 13,723–13,728, 1986.

Fejer, B. G., E. R. de Paula, R. A. Heelis, and W. B. Hanson, Global equatorial ionospheric vertical plasma drifts measured by the AE-E satellite, *J. Geophys. Res.*, *100*, 5769–5776, 1995.

Haerendel, G., J. V. Eccles, and S. Çakir, Theory for modeling the equatorial evening ionosphere and the origin of the shear in the horizontal plasma flow, *J. Geophys. Res.*, *97*, 1209–1223, 1992.

Heelis, R. A., P. C. Kendall, R. J. Moffett, and D. W. Windle, Electrical coupling of the *E* and *F* regions and its effects on *F* region drifts and winds, *Planet. Space Sci.*, *22*, 743–756, 1974.

Herrero, F. A., and H. G. Mayr, Tidal decomposition of zonal neutral and ion flows in the Earth's upper equatorial thermosphere, *Geophys. Res. Lett.*, *13*, 359–362, 1986.

Ho, C. W., T. S. Huang, and S. Gao, Contributions of the high-degree multipoles of Neptune's magnetic field: An Euler potentials approach, *J. Geophys. Res.*, *102*, 24,393–24,401, 1997.

IAGA Division V, Working Group 8, Revision of International Geomagnetic Reference Field released, *Eos Trans. AGU*, *77*(16), 153, 1996.

Maeda, H., Field-aligned current induced by asymmetric dynamo action in the ionosphere, *J. Atmos. Terr. Phys.*, *36*, 1395–1401, 1974.

Malin, S. R. C., and J. C. Gupta, The *Sq* current system during the International Geophysical Year, *Geophys. J. R. Astron. Soc.*, *49*, 515–529, 1977.

Maynard, N. C., T. L. Aggson, F. A. Herrero, and M. C. Liebrecht, Average low-latitude meridional electric fields from DE 2 during solar maximum, *J. Geophys. Res.*, *93*, 4021–4037, 1988.

Maynard, N. C., T. L. Aggson, F. A. Herrero, M. C. Liebrecht, and J. L. Saba, Average equatorial zonal and vertical ion drifts determined from San Marco D electric field measurements, *J. Geophys. Res.*, *100*, 17,465–17,479, 1995.

Richmond, A. D., Modeling the ionosphere wind dynamo: A review, *Pure Appl. Geophys.*, *47*, 413–435, 1989.

Richmond, A. D., Ionospheric electrodynamics using magnetic apex coordinates, *J. Geomagn. Geoelectr.*, *47*, 191–212, 1995a.

Richmond, A. D., The ionospheric wind dynamo: Effects of its coupling with different atmospheric regions, in *The Upper Mesosphere and Lower Thermosphere: A Review of Experiment and Theory, Geophys. Monogr. Ser.*, vol. 87, edited by R. M. Johnson and T. L. Killeen, pp. 49–65. AGU, Washington, D. C., 1995b.

Richmond, A. D., and R. G. Roble, Electrodynamic effects of thermospheric winds from NCAR thermospheric general circulation model, *J. Geophys. Res.*, *92*, 12,365–12,376, 1987.

Richmond, A. D., S. Matsushita, and J. D. Tarpley, On the production mechanism of electric currents and fields in the ionosphere, *J. Geophys. Res.*, *81*, 547–555, 1976.

Richmond, A. D., et al., An empirical model of quiet-day ionospheric electric fields at middle and low latitudes, *J. Geophys. Res.*, *85*, 4658–4664, 1980.

Richmond, A. D., E. C. Ridley, and R. G. Roble, A thermosphere/ionosphere general circulation model with coupled electrodynamics, *Geophys. Res. Lett.*, *19*, 601–604, 1992.

Stening, R. J., Calculation of electric currents in the ionosphere by an equivalent circuit method, *Planet. Space Sci.*, *16*, 717–728, 1968.

Stening, R. J., Longitude and seasonal variations of the *Sq* current system, *Radio Sci.*, *6*, 133–137, 1971.

Stening, R. J., The electrostatic field in the ionosphere, *Planet. Space Sci.*, *21*, 1897–1910, 1973.

Stening, R. J., Field-aligned currents driven by the ionospheric dynamo, *J. Atmos. Terr. Phys.*, *39*, 933–937, 1977.

Stening, R. J., A two-layer ionospheric dynamo calculation, *J. Geophys. Res.*, *86*, 3543–3550, 1981.

Takeda, M., Three-dimensional ionospheric currents and field aligned currents generated by asymmetrical dynamo action in the ionosphere, *J. Atmos. Terr. Phys.*, *44*, 187–193, 1982.

Takeda, M., Geomagnetic field variation and the equivalent current system generated by an ionospheric dynamo at the solstice, *J. Atmos. Terr. Phys.*, *52*, 59–67, 1990.

Takeda, M., and H. Maeda, Three-dimensional structure of ionospheric currents, 1, Currents caused by diurnal tidal winds, *J. Geophys. Res.*, *85*, 6895–6899, 1980.

Takeda, M., Y. Yamada, and T. Araki, Simulation of ionospheric currents and geomagnetic field variations of *Sq* for different solar activity, *J. Atmos. Terr. Phys.*, *48*, 277–287, 1986.

Tarpley, J. D., The ionospheric wind dynamo, II, Solar tides, *Planet. Space Sci.*, *18*, 1091–1103, 1970.

Vasyliunas, V. M., Mathematical models of magnetospheric convection and its coupling to the ionosphere, in *Particles and Fields in the Magnetosphere*, edited by B. M. McCormac, pp. 60–71, D. Reidel, Norwood, Mass., 1970.

Wagner, C.-U., D. Möhlmann, K. Schafer, V. M. Mishin, and M. I. Matveev, Large scale electric fields and currents and related geomagnetic variations in the quiet plasmasphere, *Space Sci. Rev.*, *26*, 391–446, 1980.

T. S. Huang and P. Le Sager, Prairie View Solar Observatory, Prairie View A&M University, P.O. Box 307, Prairie View, TX 77446, USA. (lesager@cps.pvsci.pvamu.edu)